Subsurface structure identification at the blind prediction site of ESG6 based on the earthquake-to-microtremor ratio method and diffuse field concept for earthquakes

AUTHOR(S):

Nagashima, Fumiaki; Kawase, Hiroshi; Nakano, Kenichi; Ito, Eri

Nagashima *et al. Earth, Planets and Space* (2023) 75:35
https://doi.org/10.1186/s40623-023-01791-x

Earth, Planets and Space

FULL PAPER

Open Access

Subsurface structure identification at the blind prediction site of ESG6 based on the earthquake-to-microtremor ratio method and diffuse field concept for earthquakes

Fumiaki Nagashima[1], Hiroshi Kawase[1*], Kenichi Nakano[2] and Eri Ito[1]

Abstract

We participated in the blind prediction exercise organized by the committee of the blind prediction experiment during the 6th International Symposium on Effects of Surface Geology on Seismic Motion (CBP-ESG6). In response to the committee's request, we identified the ground velocity structure from microtremors observed at a target site as the first step of the exercise. First, we calculated the horizontal-to-vertical spectral ratio of microtremors (MHVR) at the target site from the distributed microtremor data collected in the vicinity of the target site in Kumamoto Prefecture. Then, we converted the MHVR into a pseudo horizontal-to-vertical spectral ratio of earthquake (pEHVR) using the previously proposed and validated earthquake-to-microtremor ratio (EMR) method, where an empirically obtained EMR is used to convert MHVR into pEHVR. Next, we inverted the S-wave and P-wave velocity structures based on the pEHVR and the diffuse field concept for earthquakes. The theoretical EHVR calculated from the identified velocity structure reproduced the pEHVR quite well in the frequency range of 0.1–22 Hz. After the collection of the blind prediction results by all the participants, the CBP-ESG6 released the observed earthquake records, a preferred model based on the P–S logging data from the in-situ borehole measurement combined with the generic deeper structure, and the average of all the predicted structures by the participants. Notably, our inverted structure was found to be close to the preferred model and the averaged one of all the blind prediction participants, despite some minor differences in the horizontal site amplification factor around the maximum peak frequency at 0.8–1 Hz.

Keywords Diffuse field concept, Horizontal-to-vertical spectra ratio, Subsurface structure, Earthquake-to-microtremor ratio

*Correspondence:
Hiroshi Kawase
kawase@sere.dpri.kyoto-u.ac.jp
Full list of author information is available at the end of the article

Graphical Abstract

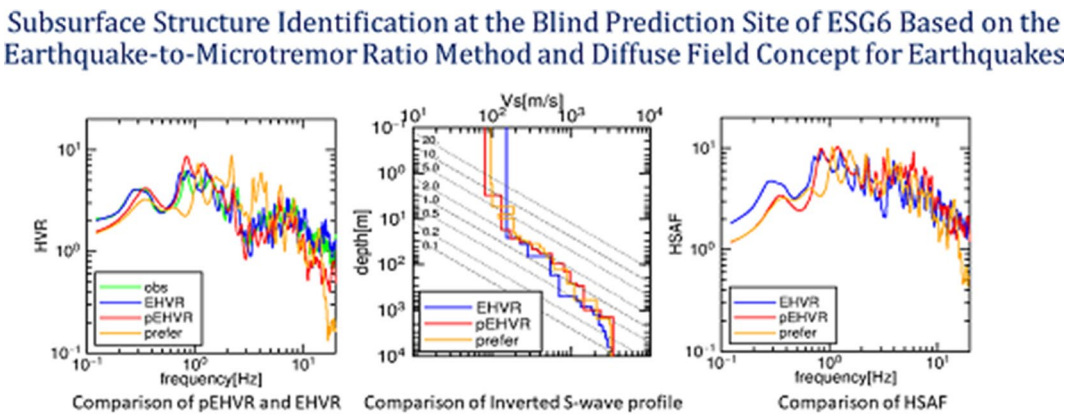

Introduction

Many schemes for identifying the subsurface structures from a priori information or in-situ observations at a target site have been previously proposed to retrieve a more realistic site amplification factor, especially for the horizontal site amplification factor (HSAF) as a function of frequency. These schemes were developed based on the empirical formulae or seismological theory-based models and subsequently applied to many different sites with different conditions. Each method has its own advantages and disadvantages, implying that the applicability of these schemes should be tailored to specific applications and that they should be validated under the same constraint conditions. Most major schemes have been previously described in two recent review papers, focused on (1) non-invasive methods of underground velocity investigations (Yong et al. 2022) and (2) the use of the Horizontal-to-Vertical spectral Ratio (HVR) to delineate the site amplification factors (Ito et al. 2020).

The committee of the blind prediction experiment during the 6th International Symposium on Effects of Surface Geology on Seismic Motion (CBP-ESG6) planned the blind prediction exercises (Matsushima et al. 2021, 2022). During the ESG6 symposium held in 2021, the purpose of the blind prediction exercises was set to provide an opportunity to research teams to validate their schemes under blind conditions. To that end, CBP-ESG6 requested participants (Step-1) to identify the ground velocity structure from the measured microtremors; (Step-2) to predict the specified aftershock motions based on the distributed observed weak motions and microtremors; and (Step-3) to predict the strong ground motions during the mainshock and foreshock of the 2016 Kumamoto earthquake (Chimoto et al. 2021, 2022; Tsuno et al. 2021, 2022). The measured velocity profile and soil nonlinearity at certain depths were distributed for Step-2 and Step-3 (Matsushima et al. 2021, 2022). We participated in all three steps of these exercises. This study describes our results identifying the velocity structure using the earthquake-to-microtremor ratio (EMR) method (Kawase et al. 2018), together with the inversion scheme based on the diffuse field concept of earthquakes (Nagashima et al. 2014), which was submitted as the result for Step-1 for the aforementioned blind prediction exercises.

The EMR method, originally proposed by Kawase et al. (2018), can estimate the pseudo horizontal-to-vertical spectral ratio of earthquake (pEHVR) from the horizontal-to-vertical spectral ratio of microtremors (MHVR) using the empirically obtained EMR. According to the diffuse field concept for earthquakes (DFCe; Kawase et al. 2011), EHVR is proportional to a ratio of the horizontal site amplification factor (HSAF) with respect to the vertical site amplification factor (VSAF) with a fixed coefficient; both amplification factors reflect the S- and P-wave velocity structures between the surface and the seismic bedrock, respectively. The theoretical EHVR based on DFCe is the key to the theoretical solution of

EHVR, thereby implying that the ground structure can be rigorously constrained by the whole spectrum of EHVR, including the higher mode peaks of both HSAF and VSAF. Although earthquakes are relatively rare, which generally implies that a long time is needed to collect a sufficient number (>10) of earthquake records, microtremors are easy to observe at all the times and we need only 15–30 min as a single-station measurement. The DFC inversion approach for MHVR was proposed by Sánchez-sesma et al. (2011) and extended by García-Jerez et al. (2016), in which MHVR was interpreted as a ratio of the imaginary parts of the horizontal and vertical Green's functions for the collocated source and receiver. The main component of microtremors is the surface wave, thereby implying that MHVR would contain sufficient information on the velocity structure near the surface. However, unlike earthquake records, it would not unveil clear contributions of higher modes of reverberated body wave within the surface and the seismological bedrock. To this end, we took advantage of both microtremors and earthquakes using microtremor measurements first and then converting MHVR to pEHVR, which has a formidable constraining power for the identification of a velocity structure based on the EHVR theory. That is what Kawase et al. (2018) have previously proposed as the EMR method, in which we convert MHVR into pEHVR by multiplying the empirical ratio of the observed EHVR over the observed MHVR (EMR), and applies DFCe to this converted pEHVR, instead of EHVR. The details of the method and its validation at 86 sites in Japan can be found in Kawase et al. (2018).

Because CBP-ESG6 asked participants to predict the velocity structure exclusively based on the observed microtremors in the blind prediction exercise of Step-1, we applied the EMR method to the target site of the blind prediction exercise, named KUMA (Matsushima et al. 2021, 2022), and identified the one-dimensional subsurface structure based on DFCe. This study shows and discusses the inverted results of the blind prediction of Step-1 and the results of the inverted structure from the observed EHVR calculated from the weak motion records, which were released after the collection of all the predictions for Step-1 and Step-2, in comparison with the results of the preferred velocity model distributed by CBP-ESG6 and the results of the average prediction. Through these comparisons, we would like to show the validity and limitation of the EMR method under the constraint conditions of the blind prediction exercise of Step-1. Please note that a preliminary report of our blind prediction results for Step-1 was submitted as an extended abstract of the ESG6 symposium and presented there as a poster (Nagashima et al. 2021), which was distributed only to the participants.

Observed MHVR and pEHVR

The CBP-ESG6 distributed the array microtremor records observed around the KUMA strong motion observation site for Step-1 (Chimoto et al. 2021, 2022). Figure 1 shows the observed MHVRs at the stations of the smallest array (SS array) with a side length of 2 m, while the distance between KUMA and the center of the array was less than 10 m. We divided all microtremor records of 45 min every 40.96 s with 50% overlapping, made the composite waveforms of three components of each divided record, calculated the sum of squares of the amplitude of the composite waveform for each divided record, and selected only 10% of the divided records with the smaller sum of squares to discard the records with

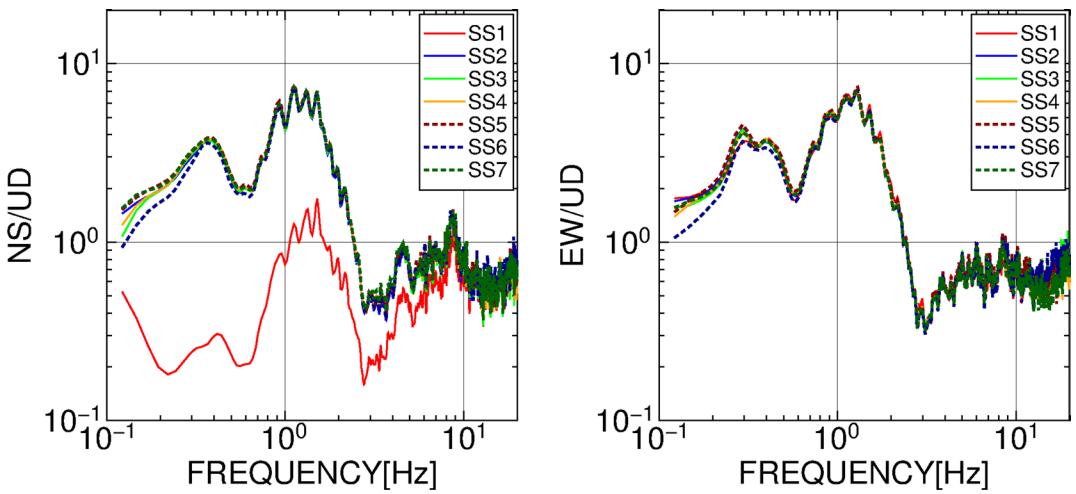

Fig. 1 Observed MHVR (NS/UD and EW/UD) of the array SS near the target site KUMA. We used the root-mean-square (RMS) values of SS2 for the analysis hereafter

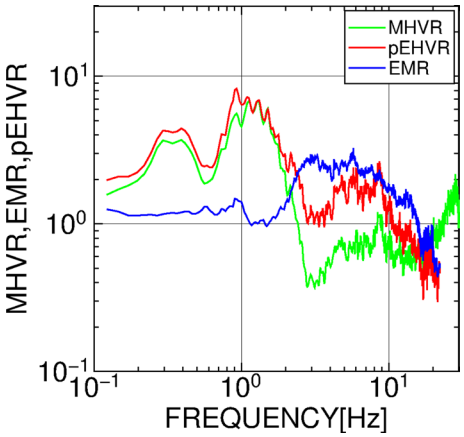

Fig. 2 Observed MHVR and converted pEHVR at the target site KUMA, together with the interpolated EMR for Category-2 used for conversion

high amplitude local noise. We subsequently applied the cosine taper to the waveforms at both ends, performed Fast Fourier Transform (FFT) for the selected records. Then, we smoothed the spectral amplitudes using the Parzen window with 0.1 Hz width, calculated the NS/UD and EW/UD ratios, and determined the geometrical means of all the used time windows. Nearly all the stations exhibited virtually the same shape of MHVR form of 0.2–20 Hz except the SS1 station, wherein a different pattern emerged for an unknown reason. The agreement of MHVRs among the stations signifies their stability and availability in this frequency range. We selected the station SS2 and obtained the root mean square (RMS) values of NS/UD and EW/UD to apply the EMR method, thereby ultimately identifying the subsurface structure.

Kawase et al. (2018) have previously obtained EMRs in five categories classified by the fundamental peak frequency of MHVR. In their classification, they used a threshold of at least 2.0 in the peak amplitude (with a clear peak characteristic in the frequency range in half and double the peak frequency), with the lowest peak frequency among multiple peaks, if any. In addition, they referred to a sharp trough and used a peak frequency around half of the trough frequency, based on the common characteristics of Rayleigh-wave ellipticity. To apply the EMR method to the MHVR observed at KUMA, we selected the fundamental peak frequency of MHVR as 1.12 Hz, thereby confirming that the EMR of Category-2 from Kawase et al. (2018) can be used, because the peak frequency of MHVR was within 1–2 Hz. Thus, we multiplied the EMR of Category-2 to the observed MHVR at SS2 to obtain pEHVR. Figure 2 shows MHVR and pEHVR, together with the EMR used to convert MHVR to pEHVR. It should be noted that the frequency axis of the original EMR, shown in Kawase et al. (2018), was normalized to the fundamental peak frequency. Accordingly, we needed to shift the frequency axis of the table by 1.12 times and performed interpolation to obtain the EMR values with the same frequency increment of MHVR (i.e., 1/40.96–0.02441 Hz). A significant correction was applied for the frequency range of > 3 Hz, which effectively made pEHVR closer to EHVR than MHVR as shown later (Fig. 4).

Subsurface structure identification

We identified the velocity structure at KUMA based on DFCe. According to DFCe, EHVR is interpreted as the ratio of the horizontal and vertical amplification factors between the ground surface and the seismic bedrock following equation (Kawase et al. 2011):

$$\frac{\mathrm{H(f)}}{\mathrm{V(f)}} = \sqrt{\frac{\alpha}{\beta}}\frac{|\mathrm{TF_{horizontal}}|}{|\mathrm{TF_{vartical}}|} \quad (1)$$

where $|\mathrm{TF_{horizontal}}|$ and $|\mathrm{TF_{vertical}}|$ are the theoretical horizontal and vertical amplification factors (i.e., the absolute value of the transfer functions), respectively, between the seismic bedrock and the ground surface for the vertical incidence of body waves, while α and β are P-wave velocity (V_p) and S-wave velocity (V_s) at the seismic bedrock, respectively. The correction coefficient as the square root of α/β is required to account for the horizontal-to-vertical amplitude ratio of the diffuse body-wave field at the seismological bedrock. For the blind prediction, we applied Eq. (1) to pEHVR obtained in the previous section to identify the subsurface structure.

To find the subsurface structure that can reproduce pEHVR, we used a hybrid heuristic searching method (HHS) originally proposed by Yamanaka (2007), which combines a real-type genetic algorithm and an anneal simulation. The details and validations for the EHVR application of HHS can be found in Nagashima et al. (2014). Our subsurface structure model for the identification consisted of 14 layers on top of a half-space, and the V_s, V_p, and thickness of these 14 layers were identified. This number of layers was set based on our previous inversion experience as the minimum number for a relatively soft site. The V_p and V_s of the half-space were fixed as 6000 m/s and 3400 m/s, respectively. The unknown values were identified without the prescribed searching range, because no a priori information was available during the blind prediction phase. However, the velocity inversion with the depth was not permitted, namely, the identified V_s and V_p should have increased with depth. The density was converted from V_s, and the constant damping of 1.1% was assumed for all the layers, as the inversions in Nagashima et al. (2014). The residual between the theoretical EHVR and pEHVR from MHVR

calculated by Eq. (2) was minimized by HHS for 216 frequency points in the frequency range from 0.1221 to 22.38 Hz, which was determined due to the minimum and maximum frequencies of pEHVR.

$$\text{Residual} = \sum \left(\log(\text{EHVR}) - \log(\text{pEHVR})\right)^2 \quad (2)$$

The calculated pEHVR was resampled to have an equal frequency increment in a logarithmic scale, and the residual amplitude was also evaluated in a logarithmic scale, so the residuals were evaluated in log–log scale for the frequency and amplitude. The generation and population for HHS were 400 and 200, respectively, while the crossing and mutation rates were set to be 0.7 and 0.1, respectively. In the HHS inversion scheme the random number was used to make the initial group of velocity structure models, to select models for the next generation, to cross the models, among others. Therefore, we identified the velocity structures ten times with the same inversion parameters for different seeds of the random number. Through this procedure, we obtained ten inversion results to evaluate the stability of the inversion by comparing these ten results. We selected the velocity model with the minimum residual among these ten inversion results as the final result.

Figure 3 shows the results of ten times inversions (i.e., theoretical EHVRs) in comparison with the observed pEHVR. The resultant V_s and V_p structures are illustrated on the right side of this figure. The black line reflects the minimum residual model among ten trials. Table 1 summarizes the details of the minimum residual model for pEHVR. We also plotted the velocity structure of the Japan Integrated Velocity Structure Model (JIVSM, Koketsu et al. 2012) at the target site and its theoretical EHVR in orange. Note that we did not have the preferred model yet during the blind prediction phase of Step-1. All our ten-time inversions reproduced pEHVR well in a wide frequency range. However, the JIVSM model could not reproduce pEHVR, except for the lowest small peak at 0.35 Hz. It should also be noted that the lowest V_s of JIVSM is fixed to be 350 m/s, because it was intended to be solely used for the long-period ground motion simulation. The ten inverted velocity structures were seemingly stable on log–log scale for both velocity and depth, and the EHVR of the best model was nearly identical to the

Table 1 Identified velocity structures for pEHVR at KUMA

No.	V_s [m/s]	V_p [m/s]	Thickness [m]	Density [kg/m^3]	Damping [%]
1	80.25	292.79	2.98	1590	0.011
2	132.09	583.95	14.14	1640	0.011
3	171.05	691.88	9.50	1680	0.011
4	224.70	691.88	5.04	1720	0.011
5	309.98	962.71	4.49	1770	0.011
6	316.74	962.71	9.27	1780	0.011
7	377.37	1242.51	6.42	1810	0.011
8	400.67	1592.47	6.06	1820	0.011
9	567.47	2184.93	39.09	1900	0.011
10	816.48	2479.75	42.99	2010	0.011
11	971.46	3489.24	116.11	2060	0.011
12	1185.42	3493.65	37.63	2130	0.011
13	1444.00	4677.22	672.66	2210	0.011
14	2357.51	5840.87	416.54	2430	0.011
15	3400.00	6000.00	–	2640	0.011

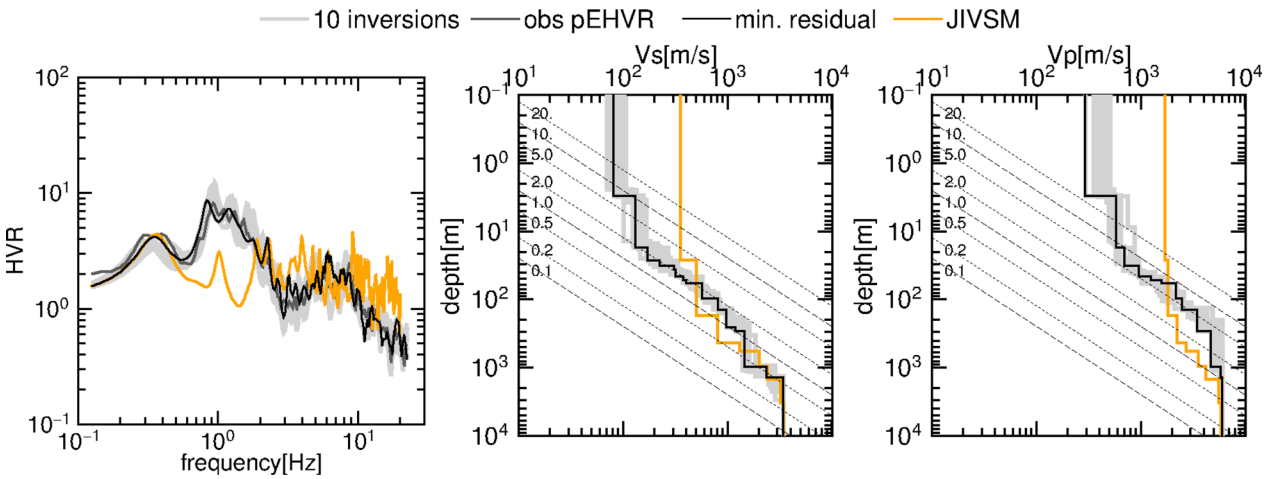

Fig. 3 Comparisons of the theoretical EHVRs by the inverted models with the observed EHVR on the left and the resultant S-wave and P-wave velocity profiles on the right. Light gray lines are the results of ten trials and the black lines are the best among them. Orange lines are those of the JIVSM structure close to KUMA (Koketsu et al. 2012). The inclined dashed and dotted lines on velocity models show resonant frequencies of the corresponding layer interfaces based on one quarter wavelength law

target pEHVR. Although the inverted V_p of the topmost layer was found to be relatively slow, the one-quarter wavelength theory for the resonant frequency (the slant dotted and broken lines) indicated that their resonant frequencies were out of the frequency band to calculate the residual (>20 Hz). Thus, this layer was considered to be poorly constrained by the target pEHVR.

Comparison of pEHVR and observed EHVR

After we submitted the velocity structure inverted for pEHVR, the Step-2 and Step-3 of the blind prediction exercise started. Then, earthquake records observed at KUMA were distributed from the CBP-ESG6 (Tsuno et al. 2021, 2022). In this section we compared the converted pEHVR from MHVR and the observed EHVR, and the inverted velocity structures from them to validate the EMR method.

In total, twelve earthquake records observed during April and May in 2016 as aftershocks of the 2016 Kumamoto earthquake were distributed for Step-2 and Step-3. The specifications of the distributed earthquakes are shown in Table 2, together with their peak ground accelerations (PGAs). We used the record sections of 40 s from the S-wave onset to calculate EHVR. The process to calculate EHVR was the same as the one that we used to calculate MHVR except for the amplitude selection applied for MHVR; we applied the cosine tapers to the 40 s waveforms at both ends, performed FFT, smoothed the spectral amplitudes by Parzen window with 0.1 Hz width, calculated the ratios of NS/UD and EW/UD, calculated the RMS values of these two ratios, and took the geometrical means of all the earthquakes. Figure 4 shows the comparison of the MHVR at SS2, the pEHVR, and the observed EHVR. All these HVRs exhibited the common peaks at around 0.35 Hz and 1 Hz, but the amplitude of

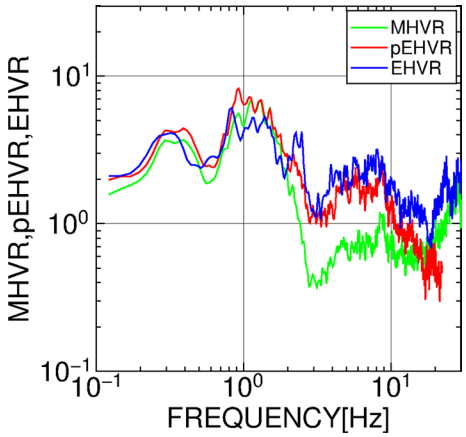

Fig. 4 Comparison of the observed MHVR, the converted pEHVR, and the observed EHVR from aftershock records disclosed after the blind prediction of Step-1 (Table 2)

EHVR was substantially larger than that of MHVR in the frequency range higher than 2 Hz. The peak amplitude of pEHVR around 1 Hz was slightly larger than that of EHVR, while a minor peak was identified at 2.3 Hz only in EHVR. The amplitude of pEHVR in the frequency range higher than 10 Hz was slightly smaller than that of EHVR. However, the EMR method can effectively correct the difference between MHVR and EHVR in general. Thus, pEHVR became very close to the observed EHVR in the frequency range of 0.1–20 Hz.

We inverted the velocity structure from the observed EHVR similar to the inversion for pEHVR. The details of the inverted velocity structure are summarized in Table 3. In the EHVR inversion we assumed the damping $h=2.5/V_s$ ($Q=V_s/5$) to obtain better matching in the high frequency range. Note that the detail of the

Table 2 Specifications of distributed earthquake data at KUMA

Origin time by JMA						Location			M	PGA (cm/s^2)		
Years	Months	Date	Hour	Minute	Second	Longitude	Latitude	Depth (km)		NS	EW	UD
2016	4	16	01	05	42.48	E130.80483	N32.71633	15.46	3.3	4.794	6.943	3.262
2016	4	16	04	05	49.20	E130.81317	N32.79733	12.29	4.0	39.454	35.737	34.932
2016	4	16	07	23	54.32	E130.77383	N32.78667	11.93	4.8	37.724	64.314	40.407
2016	4	16	11	02	51.71	E130.77817	N32.75833	14.57	4.4	48.119	99.15	827.483
2016	4	17	00	14	51.69	E131.07917	N32.96167	8.92	4.8	28.138	14.276	10.399
2016	4	17	04	46	49.09	E130.77617	N32.68717	10.32	4.5	23.034	26.068	15.394
2016	4	17	19	23	41.22	E130.72067	N32.67750	10.58	4.4	20.205	15.238	11.077
2016	4	18	08	35	43.02	E130.87333	N32.86950	10.20	4.2	11.310	12.050	6.109
2016	4	21	21	52	03.39	E130.83183	N32.78533	10.98	4.0	19.880	25.183	14.622
2016	5	05	10	31	30.47	E131.13417	N33.00033	11.16	4.6	13.744	11.286	5.422
2016	5	05	10	40	12.83	E131.12217	N32.99283	10.81	4.9	13.245	14.94	25.024
2016	5	19	02	37	44.28	E130.81417	N32.83133	16.43	3.9	13.366	23.538	13.173

Table 3 Identified velocity structures for EHVR at KUMA

No.	V_s [m/s]	V_p [m/s]	Thickness [m]	Density [kg/m^3]	Damping [%]
1	152.89	1301.22	25.74	1660	1.64
2	229.20	1301.22	9.65	1720	1.09
3	283.76	1301.22	30.42	1760	0.88
4	541.16	1562.18	18.31	1890	0.46
5	541.16	2573.38	84.46	1890	0.46
6	714.26	2954.12	322.48	1970	0.35
7	1177.63	3081.35	136.03	2130	0.21
8	1311.11	3081.35	211.61	2170	0.19
9	1832.92	3418.19	193.99	2310	0.14
10	1931.25	3470.40	188.72	2330	0.13
11	2229.58	4024.79	152.26	2400	0.11
12	2229.58	4024.79	408.70	2400	0.11
13	2229.58	4055.58	324.84	2400	0.11
14	2493.63	4382.32	225.72	2460	0.10
15	2522.22	4576.22	493.39	2460	0.10
16	2722.93	4805.46	1036.76	2510	0.09
17	2733.87	4866.3	259.89	2510	0.09
18	2955.73	5277.93	2126.65	2550	0.08
19	3319.55	5793.91	1534.06	2620	0.08
20	3400.00	6000.00	–	2640	0.07

inversion for EHVR has been described in Nagashima et al. (2022) as a part of the blind prediction in Step-2 and Step-3. We compared the inversion results for pEHVR and EHVR in Fig. 5, while also we are plotting the theoretical EHVR calculated from "the preferred model" (see Table 4) distributed by the CBP-ESG6 (Chimoto et al. 2021, 2022). In particular, it was an integrated version of the PS logging data conducted at a site close to KUMA for the shallow section down to 39 m (Matsushima et al. 2021, 2022), while the model of Senna et al. (2018) was used for the deeper part. As shown in Fig. 5, the theoretical EHVR of the inverted velocity structure from the observed EHVR very accurately reproduced the observed EHVR and the theoretical EHVR of the inverted velocity structure from pEHVR also reproduced the observed EHVR quite accurately. This finding clearly confirms the effectiveness of the EMR method. On the other hand, the preferred model with the constant 1.1% damping fails to reproduce observed EHVR. The S-wave velocity structure inverted for pEHVR was close to the preferred model, but the seismic bedrock depth of the velocity structure inverted for the observed EHVR is deeper than the depth from pEHVR (~ 1 km), thereby closely approximating to the depth of the preferred model. The difference in the deeper (> 39 m) part of the S-wave velocity (with higher velocity contrast) was found in the inversion model for EHVR. This difference of the S-wave velocity implied that the peak amplitude of ~ 0.35 Hz of EHVR exceeded that of pEHVR or the preferred model to reproduce the observed EHVR precisely in the low-frequency range. As pEHVR amplitude was slightly lower than the observed EHVR in the frequency range higher than 5 Hz (Fig. 4), the vertical amplification factor of the inversion model for pEHVR should have been larger than the inversion model for EHVR. Due to this, the shallow P-wave velocity inverted for pEHVR tended to be slower than that inverted for EHVR, thereby exacerbating the P-wave velocity contrast.

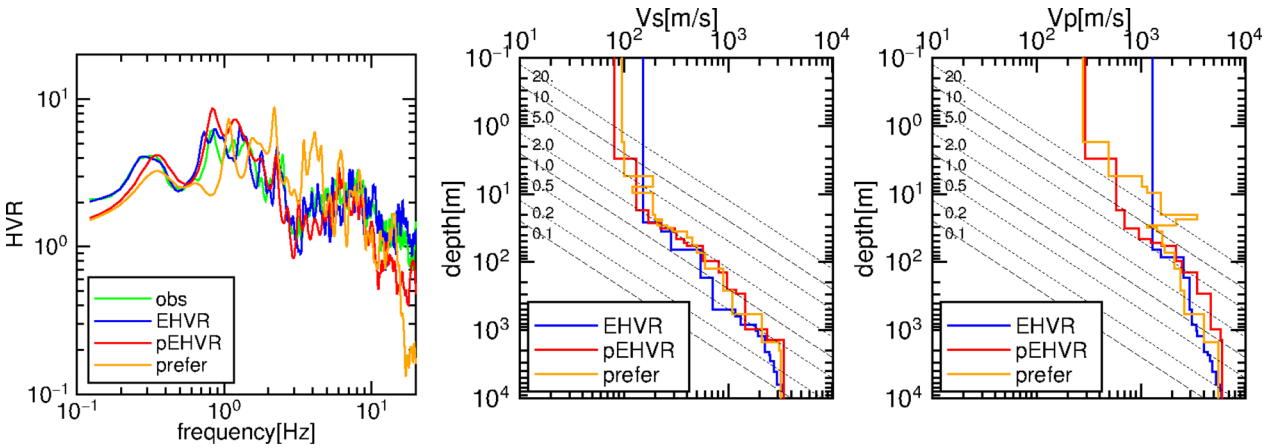

Fig. 5 Comparisons of the theoretical EHVRs by the inverted models with the observed EHVR (on the left) and the resultant S- and P-wave velocity profiles (on the right side). The red and blue lines are the result of the velocity models inverted for the converted pEHVR and the observed EHVR in Step-2, respectively, while the green line on the left is the observed EHVR. Orange lines are those of the preferred model distributed by the CBP-ESG6. The inclined dashed and dotted lines on velocity models show resonant frequencies of the corresponding layer interfaces based on one quarter wavelength law.

Table 4 Preferred model distributed by CBP-ESG6

No.	V_s [m/s]	V_p [m/s]	Thickness [m]	Density [kg/m^3]
1	95	280	1.7	1500
2	100	490	3.8	1500
3	190	1020	2.2	1600
4	120	1160	1.8	1500
5	190	1550	10.5	1600
6	200	3470	3.7	1700
7	230	2160	1.3	1700
8	210	2160	3.5	1700
9	260	1150	2.5	1700
10	290	1440	4	1700
11	400	1600	8.96	1850
12	450	1600	11.84	1850
13	500	1700	16.56	1900
14	600	2100	51.07	1900
15	900	2400	138.67	2050
16	1100	2600	317.82	2150
17	2100	4000	929.16	2400
18	3100	5500	475.57	2600
19	3200	5500	–	2650

We compared the theoretical horizontal site amplification factors (HSAFs) based on the inverted structures for EHVR or pEHVR with the theoretical HSAF from the preferred model in Fig. 6. The comparison revealed satisfactory overall matching, especially between the HSAF from pEHVR and the HSAF from EHVR. This HSAF matching simply comes from good matching in their S-wave velocity structures. The most remarkable difference between the HSAFs from the inversion and the HSAF of the preferred model was discerned in the frequency range of 0.6–0.9 Hz, where the HSAF amplitudes from the inversion exceeded that from the preferred model. This difference is seen in the left panel in Fig. 5 for EHVRs. In particular, the theoretical EHVRs from the velocity structures inverted for both EHVR and pEHVR efficiently reproduced the peak of the observed EHVR in 0.6–0.9 Hz, whereas the corresponding EHVR from the preferred model did not reproduce this peak. These correspondence of the low frequency characteristics between HSAF and EHVR (or pEHVR) strongly supports the idea of the vertical amplification correction function (VACF) proposed by Kawase et al. (2019) for pEHVR and Ito et al. (2020) for EHVR, where the empirically obtained VACF can be used to convert EHVR into HSAF. As mentioned above, VSAF from pEHVR tend to be higher in amplitude than VSAF from EHVR. The spectral shape of VSAF from the preferred model is very complicated as a manifestation of the complex P-wave velocity structure seen in the shallower part (Fig. 5).

Discussion

We compared the results of pEHVR inversion with those of EHVR inversion, specifically performed for the Step-2 blind prediction (Nagashima et al. 2022). The resultant velocity profile is considered to be the best one based on the EHVR from the observed weak motions at the target site distributed after the Step-1 and Step-2 blind prediction exercises, which were unavailable when we performed our inversion based on pEHVR for the Step-1 blind prediction. As a fair comparison between the inverted results for pEHVR and EHVR, we should use the same conditions for HHS inversion. Therefore, we show the inversion results with the same conditions for EHVR, as previously presented

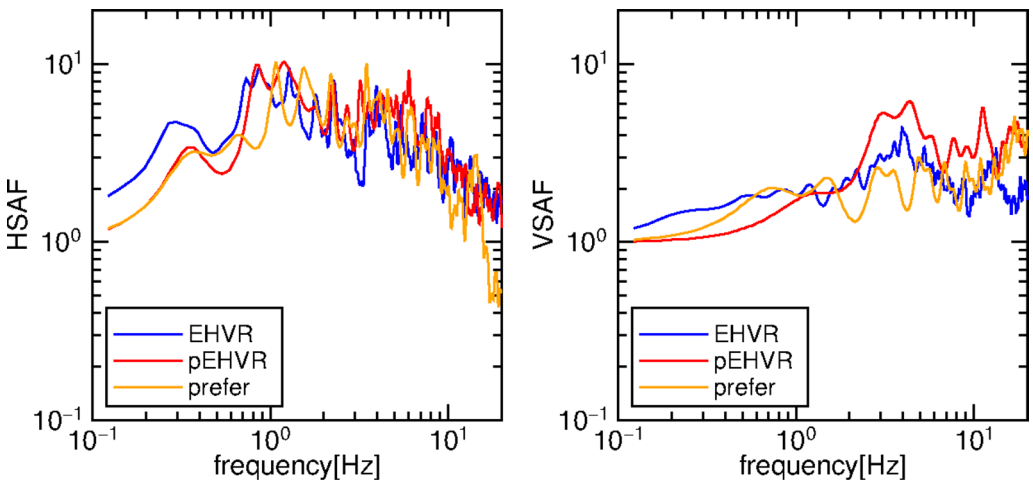

Fig. 6 Comparison of the theoretical HSAFs and VSAFs from the velocity models inverted for the converted pEHVR (red) and the observed EHVR in Step-2 (blue), together with those from the preferred model distributed by the CBP-ESG6 (orange)

(Fig. 7), using the same settings for both pEHVR and EHVR inversions. The major difference between inversion settings with pEHVR in Step-1 and EHVR in Step-2 lies in the number of layers and damping used as well as the weighting functions in the frequency (the former used equal weighting, whereas the latter used high weight in the range 0.1–0.6 Hz). Figure 7 shows comparisons of the resultant values of EHVR inversions with the settings in Step-2 and the same settings as in pEHVR inversions in Step-1 (labeled "EHVR_step1" only in Fig. 7). We noted more similarities between pEHVR and EHVR_step1 using the same settings than those between pEHVR and EHVR_step2 using different settings. The major difference in the results from EHVR inversion in Step-2 is probably attributed to high weight in the low frequency range.

Among the participants in the blind prediction exercise of Step-1 to identify the velocity structure at KUMA using the data provided (microtremor and surface exploration data) as described in Chimoto et al. (2021, 2022), we are the only research team who uses solely a single-station microtremor with the matching technique for pEHVR, that is, the converted EHVR from MHVR. After the blind prediction and the ESG6 Symposium, the CBP-ESG6 provided all the participants the average and its standard deviation distribution with depth for the S-wave velocity profiles submitted by all the participants. Please note that most other participants used array microtremor analysis methods, such as frequency-wavenumber decomposition or spatial autocorrelation method (Chimoto et al. 2021, 2022). Figure 8 shows the comparison of the average and average ± 1 standard deviation of all predictions (green) with the velocity profiles from pEHVR and EHVR (red and blue), alongside the profile of the preferred model (orange). EHVR hereafter refers to EHVR in Step 2 again. As shown here, the

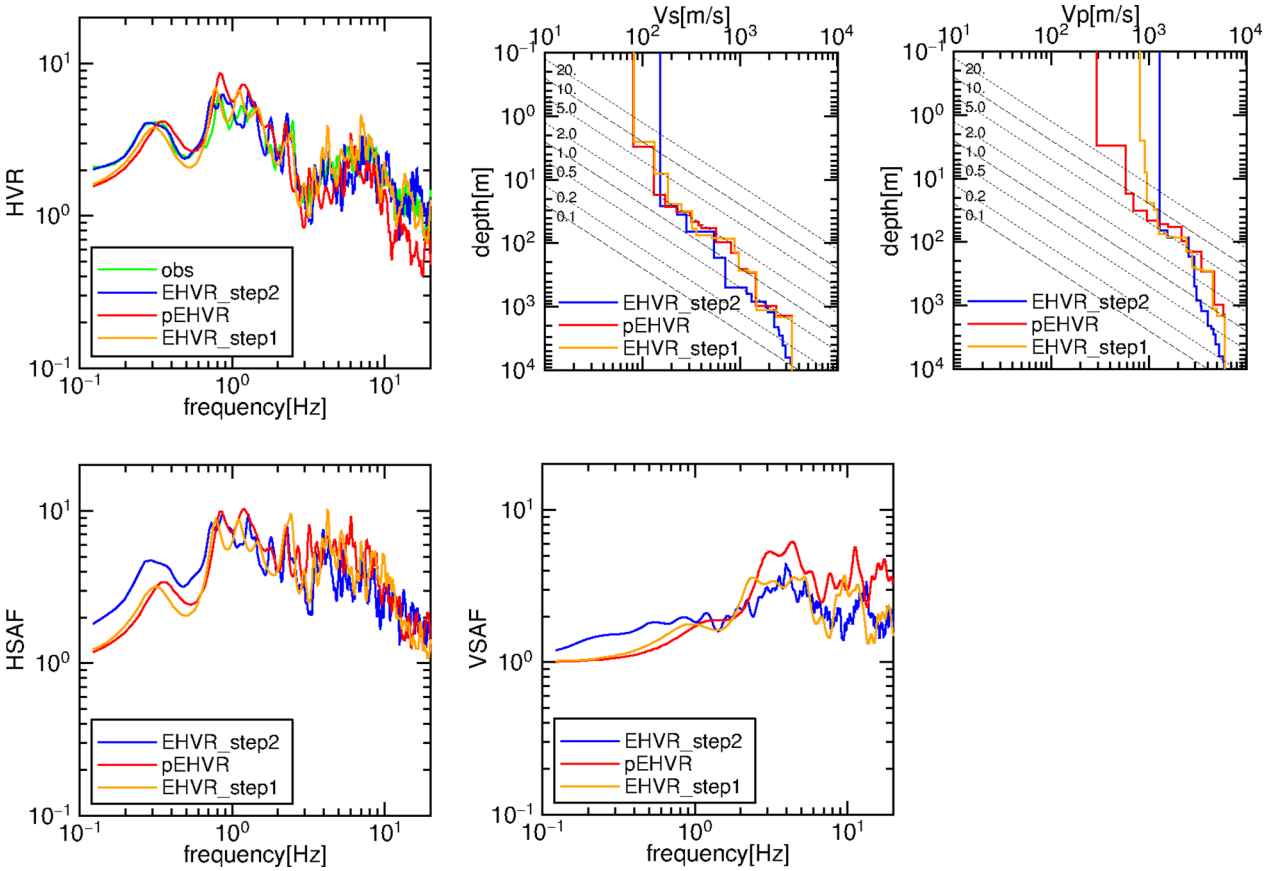

Fig. 7 Comparisons of the theoretical EHVRs by the inverted models with the observed EHVR (top row on the left) and the resultant S- and P-wave velocity profiles (top row on the right side). The red and blue lines are the results of the velocity models inverted for the converted pEHVR and the observed EHVR in Step-2 labelled as "EHVR_step2", respectively, while the green line in the top row on the left is the observed EHVR. Orange lines are those of the inverted velocity model using the same parameters as in pEHVR labelled as "EHVR_step1". In the bottom row, comparisons of the theoretical HSAFs and VSAFs from the velocity models inverted for the converted pEHVR (red) and the observed EHVR in Step-2 (blue), together with those of the inverted velocity model using the same parameters as in pEHVR, which are shown in the top row (orange). Please note that the red and blue lines are the same as those in Figs. 5 and 6

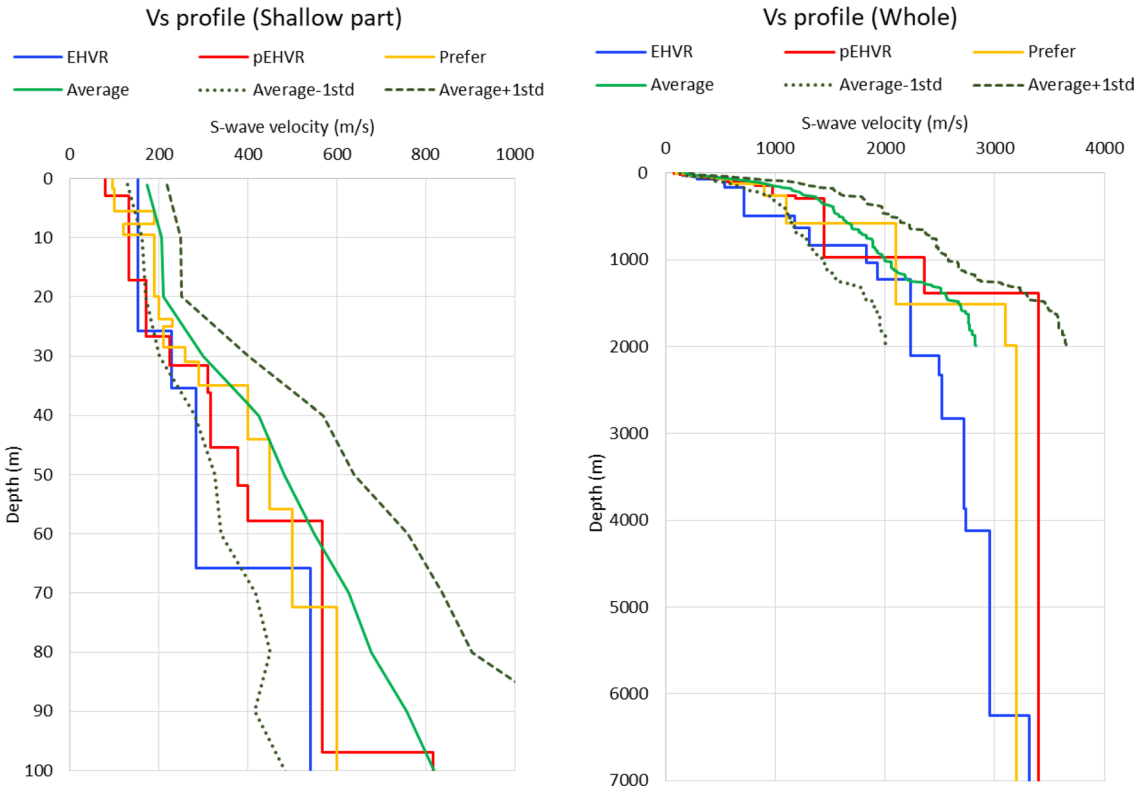

Fig. 8 Comparison of the inverted S-wave velocity profiles from pEHVR and EHVR with the average and average ± one standard deviation from all the predicted models in Step-1 (Chimoto et al. 2021). The orange line shows the profile of the preferred model

S-wave velocity profile from pEHVR fits well within the average ± 1 standard deviation, despite it being found between the average and the average -1 standard deviation range in the upper 100 m. At the same time, the profile from EHVR is running outside of the average – 1 standard deviation boundary in the depth range from 100 to 500 m. This large difference between our inversion and other predictions will show up as rather slow phase velocities in the frequency range from 1 to 2.5 Hz from our profiles if we calculate the phase velocity of the fundamental mode of Rayleigh wave from the velocity profile of the EHVR inversion, either from pEHVR or EHVR. Although the sources of this discrepancy could not be determined at this stage of analysis, we have confirmed that this average velocity structure of all the participants could not reproduce the observed EHVR as our inverted structures shown in Fig. 5.

Delineating the velocity profile underneath a target site is important for the site amplification evaluation for strong motion simulation and subsequent utilization for future disaster risk evaluations. In this context the most important value is not the detailed profile of the velocity structure itself, but rather, the resultant site amplification characteristics that will be used for strong motion evaluations. In Fig. 9, we further compared the theoretical one-dimensional HSAFs of the S-wave velocity profiles inverted for pEHVR and EHVR with the observed HSAF separated by the generalized spectral inversion technique (GIT, Nakano et al. 2015) at the closest seismic intensity observation site to KUMA, namely, EEB deployed by the Japan Meteorological Agency (JMA). The station EEB is also used for the prediction of weak and strong motions in our blind prediction exercises of Step-2 and Step-3 (Nagashima et al. 2022). We showed the locations of EEB and KUMA on the top panel, whereas we plotted the observed HASF and the theoretical HSAFs of the inverted structures, together with the theoretical HSAF of the preferred model for the reference, on the bottom panel. As shown in Fig. 9, the theoretical HSAFs from pEHVR and EHVR are similar, and both can explain the major characteristics of the observed HSAF at the closest station, although the amplitude in the high frequency range (> 4 Hz) was seemingly smaller than the observed HSAF at EEB, even when accounting for the standard deviation of the GIT estimate (approximately 1.5 times or 1/1.5 times). This is primarily because we used damping factors based on a priori assumptions

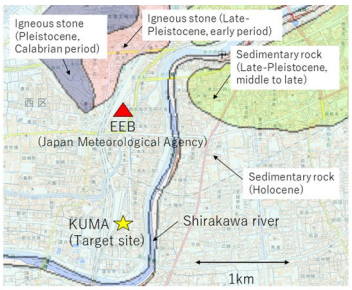

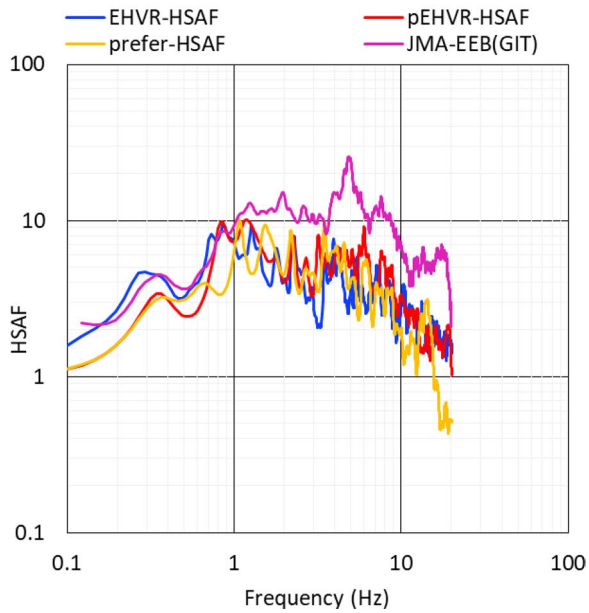

Fig. 9 Comparison of the estimated HSAF at the nearest (~ 1.2 km away) JMA station, EEB by GIT (Nakano et al., 2015), with the theoretical one-dimensional HSAFs by the inverted S-wave velocity profiles from EHVR and pEHVR, together with the HSAF by the preferred model. A geological map by Geological Survey of Japan (https://gbank.gsj.jp/seamless/) on the top shows the location of EEB relative to KUMA. The constant damping ratio of 1.1% is assumed for the pEHVR profile and preferred model, while the Vs-dependent damping (Table 3) is assumed for the EHVR profile

(either fixed as $h = 1.1\%$ for pEHVR or $h = 2.5/V_s$ for EHVR), which could be improved if we tune up these damping values. We also found that the shallow velocity structure that markedly affects the HSAF for high frequencies at EEB differs from the structure at KUMA, as presented by Nagashima et al. (2022) based on their EHVR inversion. It should be noted that all the direct HSAF comparisons between the theoretical estimates by the inverted structures and the observational one in GIT are feasible, because both of them are the absolute HSAFs from the seismological bedrock.

From these comparisons, we have successfully shown that the EMR method to obtain pEHVR from microtremors together with the HHS method for the velocity inversion from pEHVR could be a very effective combination of methods to invert the velocity structures down to the seismological bedrock only from microtremors observed at a single-station. An additional merit of obtaining pEHVR is that we can use pEHVR directly to calculate pseudo HSAF using the VACF, as proved in Kawase et al. (2019). This is theoretically supported as shown in Eq. (1) based on the DFCe and in this blind experiment, which is empirically seen in the similarity between pEHVR in Fig. 4 and HSAF from EHVR in Fig. 6.

Conclusions

We participated in the blind prediction exercise and identified the velocity structure model from the observed microtremor records based on the EMR method and DFCe inversion technique. First, we calculated MHVRs using the microtremors observed at the array microtremor stations closest to the target site of the blind prediction exercise, identified the usable frequency range by comparing the observed MHVRs at all the array sites, and calculate MHVR as a geometrical mean of the MHVRs for the selected windows. Second, we converted MHVR to pEHVR based on the EMR method for Category-2. The two predominant peak amplitudes at 0.35 and 1.0 Hz were kept intact but the amplitudes higher than 2.0 Hz were amplified by the EMR function. Finally, we applied the DFCe inversion technique to pEHVR and identified the velocity structure at the target site only from microtremors. As a result, we obtained the velocity structure that can reproduce the target pEHVR well in a wide frequency range. The comparison between the pEHVR and the observed EHVR that were later disclosed demonstrated that the pEHVR was very close to the observed EHVR, despite their detailed characteristics at the maximum peak and in the higher frequency range differed. The difference affected the inversion results of the horizontal amplification factor calculated from the S-wave velocity, and the vertical amplification factor calculated from the P-wave velocity. The characteristics of the HSAF from the inverted velocity structures were found to be close to those of the HSAF from the preferred model distributed by the organizers. However, the residual from the observed EHVR was apparently smaller for the EHVR of the inverted structures, either from EHVR or pEHVR, than for the EHVR of the preferred model. Considering the good correlation of the spectral shapes between EHVR and HSAF, the velocity structure that can reproduce EHVR would be better to be used for HSAF evaluation for strong motion

simulation. The reproducibility of HSAF by the inverted structure was somehow confirmed by comparing the observed HSAF at the nearest JMA station, where we obtained the separated HSAF from the observed records by GIT. It would be interesting in future to invert the damping factors that could reproduce the HSAF separated by GIT.

Abbreviations

CBP	The committee of the blind prediction experiment
GIT	Generalized spectral inversion technique
DFCe	Diffuse field concept for earthquake
EMR	Earthquake-to-microtremor ratio (Carriage Return)
EHVR	Earthquake horizontal-to-vertical spectral ratio
ESG6	The 6th International Symposium on Effects of Surface Geology on Seismic Motion (Carriage Return)
HSAF	Horizontal site amplification factor
JIVSM	Japan Integrated Velocity Structure Model
JMA	Japan Meteorological Agency
MHVR	Microtremor horizontal-to-vertical spectral ratio
pEHVR	Pseudo earthquake horizontal-to-vertical spectral ratio
VACF	Vertical amplification correction function
VSAF	Vertical site amplification factor

Acknowledgements
The collection and distribution of the data for the blind prediction by the CBP-ESG6 is highly appreciated, without which this research could not be conducted. Especially, unselfish effort by Prof. Matsushima, Prof. Yamanaka, Prof. Chimoto, and Dr. Tsuno should be greatly acknowledged. We would like to thank Editage (www.editage.com) for English language editing.

Author contributions
The main strategy of the investigation was determined through the discussion of HK, FN, and EI. The velocity inversions were performed primarily by FN using the HHS code developed by FN. HSAFs by GIT was obtained and provided by KN. The work for the discussion section was performed by EI, HK, and NF through the discussion with KN. All authors contributed to editing and revising the manuscript. All authors read and approved the final manuscript.

Funding
This work was partially supported by the JSPS Grant-in-Aid for Basic Research (B) No.19H02405 (P.I.: Hiroshi Kawase). Support for the laboratory of Sophisticated Earthquake Risk Evaluation from Hanshin Consultants Co. Ltd. is highly appreciated.

Availability of data and materials
Microtremor and earthquake records at and around the KUMA site were provided by the CBP-ESG6 specifically to the blind prediction participants. Earthquake records at EEB are distributed by Japan Meteorological Business Support Center at http://www.jmbsc.or.jp/en/index-e.html (last accessed 2022/09/15). Boring log data and dynamic deformation characteristics were reported in Matsushima et al. (2021, 2022) as a part of the activities of the CBP-ESG6. All the other data generated during this study can be disclosed upon request.

Declarations

Ethics approval and consent to participate
Yes, we all have checked and approved.

Consent for publication
All authors have agreed to the publication of the manuscript.

Competing interests
The authors declare that they have no competing interests.

Author details
[1]DPRI, Kyoto University, Gokasho, Uji, Japan. [2]HAZAMA-ANDO CORP., Karima, Tsukuba 515-1, Japan.

Received: 25 September 2022 Accepted: 23 February 2023
Published online: 13 March 2023

References

García-Jerez A, Piña-Flores J, Sánchez-Sesma FJ, Luzón F, Perton M (2016) A computer code for forward calculation and inversion of the H/V spectral ratio under the diffuse field assumption. Comp Geosci 97:67–78

Ito E, Nakano K, Nagashima F, Kawase H (2020) A method to directly estimate S-wave site amplification factor from horizontal-to-vertical spectral ratio of earthquakes (eHVSRs). Bull Seismol Soc Am 110(6):2892–2911. https://doi.org/10.1785/0120190315

Kawase H, Sanchez-Sesma FJ, Matsushima S (2011) The optimal use of horizontal-to-vertical spectral ratios of earthquake motions for velocity inversions based on diffuse-field theory for plane waves. Bull Seismol Soc Am 101(5):2001–2014. https://doi.org/10.1785/0120100263

Kawase H, Mori Y, Nagashima F (2018) Difference of horizontal-to-vertical spectral ratios of observed earthquakes and microtremors and its application to S-wave velocity inversion based on the diffuse field concept. Earth Planets Space 70:1. https://doi.org/10.1186/s40623-017-0766-4

Nagashima F, Matsushima S, Kawase H, Sánchez-Sesma FJ, Hayakawa T, Satoh T, Oshima M (2014) Application of horizontal-to-vertical (H/V) spectral ratios of earthquake ground motions to identify subsurface structures at and around the K-NET site in Tohoku, Japan. Bull Seismol Soc Am 104(5):2288–2302

Sánchez-Sesma FJ, Rodríguez M, Iturrarán-Viveros U, Luzón F, Campillo M, Margerin L, García-Jerez A, Suarez M, Santoyo MA, Rodríguez-Castellanos A (2011) A theory for microtremor H/V spectral ratio: application for a layered medium. Geophys J Int 186:221–225. https://doi.org/10.1111/j.1365-246X.2011.05064.x

Senna S, Wakai A, Suzuki H, Yatagai A, Matsuyama H, Fujiwara H (2018) Modeling of the subsurface structure from the seismic bedrock to the ground surface for a broadband strong motion evaluation in Kumamoto Plain. J Disast Res 13(5):917–927

Yamanaka H (2007) Inversion of surface-wave phase velocity using hybrid heuristic search method. BUTSURI-TANSA 60(3):265–275. https://doi.org/10.3124/segj.60.265(inJapanese)

Yong A, Askan A, Cassidy J, D'Amico S, Parolai S, Pilz M, Stephenson W (2022) Introduction to the special issue of the consortium of organizations for strong motion observation systems (COSMOS) international guidelines for applying noninvasive geophysical techniques to characterize seismic site conditions. J Seismol 26:557–566. https://doi.org/10.1007/s10950-022-10104-w

Chimoto K, Yamanaka H, Tsuno S, Shigefuji M, Kanno T, Sato H, Higashi S, Shinoyama D, Yoshimi M, Sugiyama T, Takai N, Matsushima S, Nagashima F, Kawase H, Hayakawa T, Uetake T, Senna S, Inagaki Y, Hayashida T, Oji S (2021) Results of blind prediction Step 1: subsurface velocity structure model of Kumamoto Test Site. In: Proceedings of the 6th IASPEI/IAEE international symposium on effects of surface geology on seismic motion, Kyoto University, Uji, Japan, 31 August–2 September 2021, SS102-BP1.

Chimoto K, Yamanaka H, Tsuno S, Matsushima S (2022) Predicted results of the velocity structure at the target site of the blind prediction exercise from microtremors and surface wave method as Step-1, -Report of the experiments for "The 6th International Symposium on Effects of Surface Geology on Seismic Motion". Earth Planets Space (under revision).

Kawase H, Nagashima F, Nakano K, Mori Y (2019) Direct evaluation of S-wave amplification factors from microtremor H/V ratios: double empirical corrections to "Nakamura" method. Soil Dyn Earthq Eng. https://doi.org/10.1016/j.soildyn.2018.01.049

Koketsu K, Miyake H, Suzuki H (2012) Japan integrated velocity structure model version 1. In: Proceedings of 15th World Conf on Earthq Eng, Lisbon, Portugal, Paper No. 1773.

Matsushima, S, Yamanaka H, Tsuno S, Sato H, Inagaki Y (2021) Results of borehole survey at the target site of ESG6 blind prediction exercise and laboratory tests. In: Proceedings of the 6th IASPEI/IAEE international

symposium on effects of surface geology on seismic motion, Kyoto University, Uji, Japan, 31 August–2 September 2021, SS101.
Matsushima S, Yamanaka H, Tsuno S, Chimoto K, Suzuki H, Kawase H (2022) Investigation of the subsurface structure at the target site in Kumamoto, Japan and the distributed data of the blind prediction exercise, -Report of the experiments for "The 6th International Symposium on Effects of Surface Geology on Seismic Motion". Earth Planets and Space (under revision).
Nagashima F, Kawase H, Nakano K, Ito E (2021) Subsurface structure identification based on EMR method and diffuse field concept for earthquake. In: Proceedings of the 6th IASPEI/IAEE international symposium on effects of surface geology on seismic motion, Kyoto University, Uji, Japan, 31 August–2 September 2021, SS11-P05.
Nagashima, F, Kawase H, Nakano K, Ito E (2022) Application of ground motion prediction method based on diffuse field concept for earthquake. Earth, Planet Space (under revision).
Tsuno S, Kawase H, Yamanaka H, Matsushima S, Iwata T, Hayakawa T, Ikeura T, Noguchi S, Kaneda K (2021) Results of blind prediction Step 2: Simulation of weak motions observed at the Kumamoto Test Site and results of blind prediction Step 3: Simulation of strong motions observed at the Kumamoto Test Site. In: Proceedings of the 6th IASPEI/IAEE international symposium on effects of surface geology on seismic motion, Kyoto University, Uji, Japan, 31 August–2 September 2021, SS103-BP3.
Tsuno S, Nagashima F, Kawase H, Yamanaka H, Matsushima S (2022) Predicted results of the weak and strong ground motions at the target site of the blind prediction exercise as Step 2 and Step-3, -Report of the experiments for "The 6th International Symposium on Effects of Surface Geology on Seismic Motion". Earth Planets and Space (under revision).
Nakano K, Matsushima S, Kawase H (2015) Statistical properties of strong ground motions from the generalized spectral inversion of data observed by K-NET KiK-net and the JMA Shindokei Network in Japan. Bull Seismol Soc Am 105(5) 2662-2680 10.1785/0120140349

Publisher's Note